

# Wideband MIMO Frequency Modulated Emission Design with Space-Frequency Nulling

Patrick M. McCormick, *Student Member, IEEE*, Shannon D. Blunt, *Fellow, IEEE*,  
and Justin G. Metcalf, *Member, IEEE*

**Abstract**—A design approach is presented that jointly optimizes the beampattern and spectral content of a wideband MIMO radar emission within the context of physically realizable frequency-modulated (FM) waveforms emitted from a uniform linear array. Such waveforms minimize the distortion induced by the power amplifier by virtue of being constant amplitude and inherently well-contained spectrally. The design approach is a specific form of alternating projections that shapes the emission spectrum as a function of spatial angle while intrinsically addressing the problem of reactive power that arises for the wideband MIMO emission. This scheme also permits incorporation of joint space-frequency nulling to facilitate spectrum cohabitation with other nearby RF users. The design process is performed in a discretized manner that is over-sampled relative to waveform 3-dB bandwidth to capture a sufficient portion of the spectral roll-off to realize the physical waveform, which is subsequently implemented via the polyphase-coded FM (PCFM) structure.

**Index Terms**—Multiple-Input multiple-output (MIMO) radar, wideband, beampattern optimization.

## I. INTRODUCTION

WITHIN the broader context of waveform diversity [1]–[4], the design of MIMO radar emissions is typically approached from a narrowband perspective where the steering vectors of the array are constant throughout the bandwidth of the emission [5]–[7]. The optimal power allocation in space for traditional wideband emissions has also been investigated [8], [9]. Likewise in [10], the wideband MIMO beampattern was optimized using the relationship between the beampattern and the cross-spectral density matrix. In [11] the waveform matrix was obtained by first determining the optimal waveform spectra (in a least-squares sense) that matches a desired space-frequency beampattern and then optimizing the waveform matrix in the time-domain given a PAPR constraint.

Here an iterative wideband MIMO waveform design scheme is presented that is an extension of the method introduced in [12] where the spectrum in certain transmission angles,

denoted as “beamlets”, are shaped according to a predefined spectral window that includes a sufficient portion of the spectral roll-off region. In so doing, physical waveforms can be realized in a discretized fashion that a) are constant amplitude and spectrally well-contained so as to be robust to the distortion induced by the transmitter power amplifier, b) minimize the reactive power otherwise generated by wideband MIMO emissions, and c) can be readily implemented with high fidelity via the polyphase-coded FM (PCFM) framework [13].

As an extension to [12], space-frequency nulling is incorporated into the emission design to facilitate coexistence with other spectrum users in the vicinity of the radar. The space-frequency beampattern matching problem from [12] cannot produce nulls of sufficient depth, thus an additional stage is needed to enforce null constraints. To do so, the reiterative uniform weight optimization (RUWO) method [22] is included within the larger emission design scheme. Analysis of the overall design process is presented to evaluate emission correlation, calculation of reactive power, and convergence behavior.

The proposed design scheme leverages the body of work on phase retrieval algorithms (e.g. [14]–[19]) which typically do not have closed form solutions but can be solved using iterative transform methods generally referred to as alternating projections. Such methods have been shown to be effective to synthesize polyphase codes via shaping of the power spectral density (PSD) [19]. Similar methods have likewise been recently shown to facilitate the optimization of frequency modulated (FM) waveforms [20], [21]. Typically, signal synthesis algorithms of this type possess sets of constraints in two domains referred to as the *object* and *image* domains. A solution is found by alternating between the two domains, enforcing the constraints during each stage. For this joint space/frequency formulation, the object domain is element-time, with a constant amplitude constraint on the waveform generated by each of the  $M$  array elements. The image domain is space-frequency, with the far-field emission constrained to particular spatial directions (the “beamlets”) with predefined spectral windows.

To address the physical nature of a wideband MIMO emission, the amount of energy stored due to “radiating” into the invisible space is considered [23]–[25]. This energy, which can lead to large amounts of reflected power, typically is associated with reactive power and occurs in arrays with electrical spacing that is less than a half-wavelength, which may correspond to a large portion of the bandwidth of a wideband emission. It is shown that the proposed emission

Copyright (c) 2016 IEEE. Personal use of this material is permitted. However, permission to use this material for any other purposes must be obtained from the IEEE by sending a request to pubs-permissions@ieee.org

This work was supported by a subcontract with Matrix Research, Inc. for research sponsored by AFRL under Prime Contract # FA8650-14-D-1722.

Patrick M. McCormick is with the Electrical Engineering & Computer Science Department, University of Kansas, 1520 W. 15th St., Lawrence, KS, 66045 USA (e-mail: pmccormick@ittc.ku.edu)

Shannon D. Blunt is with the Electrical Engineering & Computer Science Department, University of Kansas, 1520 W. 15th St., Lawrence, KS, 66045 USA (e-mail: sdblunt@ittc.ku.edu)

Justin G. Metcalf is with the U.S. Air Force Research Lab (AFRL), Sensors Directorate, 2241 Avionics Circle, Wright-Patterson Air Force Base, OH 45433 USA (e-mail: justin.metcalf@us.af.mil)

design effectively mitigates the energy contained in this region ensuring the spatial angles of the beamlets reside within the visible space. The *fractional reactive power* (FRP) metric is defined to measure the percentage of power imparted to this region.

To demonstrate the utility of this approach three wideband emission scenarios are considered: 1) three spatially separated narrow beams (e.g. to track multiple targets in different spatial directions simultaneously), 2) a near omnidirectional wide beam comprised of many closely-spaced beamlets (e.g. for SAR applications [26]), and 3) a moderately wide beam concurrent with a narrow secondary beam in a different spatial direction (e.g. for multi-mode operation [27]). Each case includes one to two space-frequency nulls that encompass large regions in space-frequency. For each scenario, the frequency content of the designed emission and spatial beampattern are presented along with convergence plots, correlation analysis, and determination of the FRP.

The remainder of the paper is organized as follows. In Section II the physical realization of a wideband MIMO emission is considered. In Section III wideband array analysis is presented along with definitions of bandwidth, the invisible space, and wideband beamforming. The wideband MIMO emission design with space-frequency nulling is then presented in Section IV, with Section V briefly outlining the continuous-time, polyphase-coded frequency-modulated (PCFM) implementation of the resulting waveform matrix. Finally, in Section VI the three different example scenarios are described and results analyzed.

## II. PHYSICAL CONSIDERATIONS

For any emission optimization involving multiple antenna elements the physical electromagnetic interaction between these elements needs to be considered. This *mutual coupling* interaction can be described using a frequency-dependent mutual impedance between each pair of antennas just as every antenna has a frequency-dependent self-impedance. The coupling of antennas directly alters the driving impedances of the antenna elements and is dependent on the amplitude and phase of the array excitation and frequency of the transmission [28]. The spatially-dependent impedance variation can be decreased by placing antenna elements closer together [29]. However, large reflections can occur if the electrical spacing between elements becomes less than a half-wavelength for a given frequency such that the emission “radiates” into what is known as the invisible (or imaginary) space [23]. The term “radiate” is really a misnomer in this context as the majority of the power is actually not radiated due to the element drive impedance becoming largely reactive. The result is storage of energy locally in the near field of the array, which can lead to large amounts of reflected power that could damage the transmitter [23], [25]. The invisible space is leveraged in the design of super-directive array patterns, which are known to store large amounts of energy [30].

This “reactive” region resides beyond the endfire direction for linear arrays and does not correspond to a physical angular direction. For wideband arrays, the frequency-dependence of

the electrical spacing between antenna elements becomes significant and cannot be assumed a constant over the bandwidth. Thus the ratio of invisible to visible space changes over the bandwidth of the emission. A more thorough description of visible and invisible space is presented in Section III-D.

The angular-dependent element impedance variation can also result in what is known as *scan blindness* where the mismatch between the transmitter and antenna is such that little to no power is transmitted in a particular transmit angle. These directions have been linked to angles at which a grating lobe appears in real space but can occur at smaller angles as well [31]. In this paper, the assumption is made that the array is matched (no reflections) over all visible space and completely mismatched (total reflection) in invisible space. Therefore, while the “radiation” of power into the invisible space is addressed, the phenomenon of scan blindness is considered outside the scope of the current work. Such mutual coupling dependent effects for MIMO, e.g. [32], [33], will be considered elsewhere.

## III. WIDEBAND ARRAY ANALYSIS

When considering wideband signals many assumptions that are made for narrowband signals become invalid. Two well-known methods of wideband beamforming [34] are discrete Fourier transform (DFT) beamforming, where frequency-dependent steering vectors are applied in the Fourier domain, and finite impulse response (FIR) beamforming, where an FIR filter is placed at the output of each antenna element. Both methods employ true-time delay processing, which is necessary for wideband signals. The method of DFT beamforming is adopted here.

### A. Bandwidth definition

Bandwidth is typically defined within a certain power level (e.g. 3-dB), or bounded by a percentage of total power (e.g. 98% of total power). When considering different spectral shapes the “percentage of total power” definition of bandwidth is attractive as it accounts for spectral roll-off and limits the amount of power in the roll-off region to a percentage of the total.

For example, Fig. 1 shows both a Gaussian spectrum and the spectrum of a linear frequency modulated (LFM) waveform that have identical 3-dB bandwidths. The powers outside the bandwidth for these spectra represent 24% and 5.5% of the total power, respectively.

In contrast, Fig. 2 shows a Gaussian spectrum and LFM spectrum with equal 98% power bandwidths. In so doing the spectra are normalized to have equal in-band power, and thus equal out-of-band power. They are visually more comparable in spectral shape, as well. We shall use this definition of bandwidth for emission design.

Note that the percent power bandwidth definition becomes ambiguous when considering nulled spectra. Thus, assuming that nulling is applied to a base spectral shape, we shall define the bandwidth of the nulled spectrum according to this base spectral shape prior to nulling.

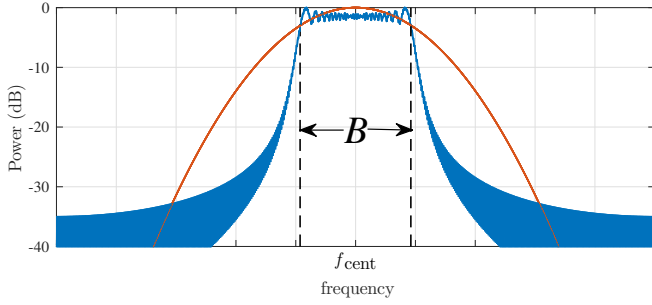


Fig. 1. 3-dB bandwidth for Gaussian spectral shape (red) and linear frequency modulated waveform (blue).

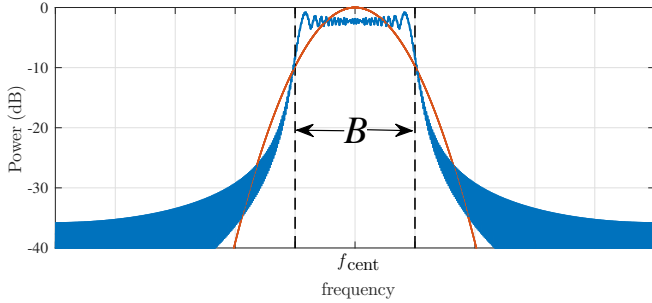


Fig. 2. 98% power bandwidth for Gaussian spectral shape (red) and linear frequency modulated waveform (blue).

### B. Wideband beamforming

Consider an  $M$  element uniform linear array (ULA) with element spacing  $d$ . For a narrowband array, the complex-baseband far-field emission as a function of time  $t$  and spatial angle  $\theta$  can be defined as

$$h(t, \theta) = \frac{1}{M} \sum_{m=0}^{M-1} s_m(t) e^{jm\phi(\theta)}, \quad (1)$$

where  $s_m(t)$  is the complex-baseband representation of the continuous, pulsed waveform emitted by the  $m$ th antenna element and  $\phi(\theta)$  is the electrical angle defined as

$$\phi(\theta) = \frac{2\pi}{\lambda_{\text{cent}}} d \sin \theta, \quad (2)$$

for  $\lambda_{\text{cent}}$  the wavelength of  $f_{\text{cent}}$  the center frequency. If the element spacing  $d$  is defined as half of wavelength  $\lambda_d$  corresponding to some frequency  $f_d$  as

$$d = \frac{\lambda_d}{2} = \frac{c}{2f_d} \quad (3)$$

for  $c$  the speed of light, the electrical angle  $\phi$  can be rewritten as

$$\phi(\theta) = \pi \frac{f_{\text{cent}}}{f_d} \sin \theta. \quad (4)$$

This form is convenient when generalizing the electrical angle for a wideband emission.

For wideband arrays, the electrical angle becomes dependent on the continuous passband frequency  $f$  as

$$\phi(f, \theta) = \pi \frac{f}{f_d} \sin \theta. \quad (5)$$

Because of the frequency dependence, the electrical phase shift is applied to the signals in the Fourier domain, such that the complex-baseband emission as a function of passband frequency  $f$  and spatial angle  $\theta$  becomes

$$g(f, \theta) = \frac{1}{M} \sum_{m=0}^{M-1} \left[ \int_0^T s_m(t) e^{-j2\pi(f-f_{\text{cent}})t} dt \right] e^{jm\phi(f, \theta)}. \quad (6)$$

Note that the frequency  $f$  in (6) is the average response over pulsewidth  $T$  (as opposed to instantaneous frequency). Taking the inverse Fourier transform of (6) yields

$$\begin{aligned} h(t, \theta) &= \frac{1}{M} \sum_{m=0}^{M-1} s_m(t) * \delta \left( t + \frac{m}{2f_d} \sin \theta \right) \\ &= \frac{1}{M} \sum_{m=0}^{M-1} s_m \left( t + \frac{m}{2f_d} \sin \theta \right) \end{aligned} \quad (7)$$

for  $*$  convolution. The complex envelope of the far-field emission, given by (7), is a summation of time-shifted waveforms in which delay is dependent on the spatial angle  $\theta$  and is relative to element 0.

Now consider an  $N \times M$  discretized complex-baseband waveform matrix  $\mathbf{S}$  in which the columns correspond to the waveforms emitted by each of the  $M$  antenna elements, with  $N$  the length of the discretized waveforms in the time domain. The matrix can be vectorized into an  $MN \times 1$  vector  $\mathbf{s}$  where the waveforms are stacked starting with the leftmost waveform vector. To adequately represent these continuous waveforms in discrete form, it is necessary to "over-sample" with respect to some bandwidth measure so as to capture an adequate portion of the spectral roll-off (which is theoretically infinite due to the pulsed nature of the signal). Thus the complex-baseband emission as a function of passband frequency  $f$  and spatial angle  $\theta$  from (6) can be well approximated as

$$g(f, \theta) = \frac{1}{M} [\mathbf{t}(f, \theta)]^H \mathbf{s} \quad (8)$$

where  $(\bullet)^H$  is the conjugate-transpose. The  $MN \times 1$  space-frequency steering vector

$$\mathbf{t}(f, \theta) = \mathbf{v}(f, \theta) \otimes \mathbf{a}(f), \quad (9)$$

for frequency  $f$  and spatial angle  $\theta$  with  $\otimes$  the Kronecker product, is comprised of the  $M \times 1$  frequency-dependent steering vector

$$\mathbf{v}(f, \theta) = [ 1 \quad e^{-j\phi(f, \theta)} \quad \dots \quad e^{-j(M-1)\phi(f, \theta)} ]^T \quad (10)$$

and the  $N \times 1$  discrete-time Fourier transform (DTFT) vector

$$\mathbf{a}(f) = [ 1 \quad e^{j2\pi \frac{f-f_{\text{cent}}}{f_{\text{samp}}}} \quad \dots \quad e^{j2\pi(N-1) \frac{f-f_{\text{cent}}}{f_{\text{samp}}}} ]^T \quad (11)$$

as a function of continuous passband frequency  $f$ , for  $f_{\text{samp}}$  the sampling rate of the discretized waveforms in  $\mathbf{S}$ .

Since it is impossible to represent this beamformer as a continuous frequency spectrum using digital signal processing, the spectrum is discretized and a discrete Fourier transform (DFT) is used to transform the signal into the discretized frequency domain. This type of beamforming is known as the DFT beamformer for wideband arrays [34].

Discretizing the frequency spectrum into  $Q$  equally spaced points, define the discrete baseband frequencies as

$$f_q = \frac{-f_{\text{samp}}}{2} + \frac{q}{Q}f_{\text{samp}} \quad (12)$$

for  $q = 0, 1, \dots, Q - 1$ . Therefore the discrete passband frequency becomes

$$f = f_q + f_{\text{cent}}. \quad (13)$$

Inserting (12) and (13) into (11) yields the  $N \times 1$  DFT vector at discrete baseband frequency  $f_q$  as

$$\mathbf{a}(f_q) = \left[ 1 \quad e^{j2\pi(-\frac{1}{2} + \frac{q}{Q})} \quad \dots \quad e^{j2\pi(N-1)(-\frac{1}{2} + \frac{q}{Q})} \right]^T. \quad (14)$$

To account for the time delay in wideband beamforming the number of frequency points  $Q$  needs to be over-specified relative to  $N$ , the discretized length of the waveform, to prevent aliasing of the complex envelope of the emission. This over-specified frequency representation corresponds to a zero-padding in the time-domain to account for the possible sample delays that may occur. The number of additional samples necessary is dictated by the maximum sample shift  $\lceil f_{\text{samp}} \Delta\tau_{\text{max}} \rceil$ , where  $\lceil \bullet \rceil$  is the ceiling operation and  $\Delta\tau_{\text{max}}$  is the maximum time delay between any two elements in the array. Therefore, the number of frequency points must meet or exceed the discrete length of the waveform plus this maximum sample shift, or  $Q \geq N + \lceil f_{\text{samp}} \Delta\tau_{\text{max}} \rceil$ . The discrete length of the waveform can be represented in terms of the sampling frequency  $f_{\text{samp}}$  and the pulse duration  $T$  as

$$N = f_{\text{samp}}T \quad (15)$$

and the maximum delay

$$\Delta\tau_{\text{max}} = \frac{M-1}{2f_d}, \quad (16)$$

is the largest delay term from (7). Therefore, the number of frequency points  $Q$  must adhere to

$$Q \geq N + \left\lceil f_{\text{samp}} \left( \frac{M-1}{2f_d} \right) \right\rceil \quad (17)$$

to prevent aliasing of the complex envelope. As shown in (7), the wideband emission is numerically equivalent to a summation of the waveforms emitted from each element convolved with delayed impulse functions. Since the waveforms are sampled, the impulse function is represented as a truncated sinc function, thus the time-shifted waveform will exhibit the well-known Gibbs phenomenon that produces time sidelobes beyond the extent of the pulsewidth [35]. Increasing  $Q$  above the bound in (17) extends the time window, thus reducing error due to aliasing of these sidelobes. It has been observed that  $Q = 2N$  frequency points are sufficient to reduce this error to a negligible amount.

### C. Wideband definition and the narrowband assumption

For a signal impinging on or emitted from an array, the methods used to define whether a signal is narrowband depends not only on the spectral content of the signal but also on the geometry of the array. As a result, there are two distinct

narrowband definitions: one that we shall call the *spectral* narrowband definition and the other the *array* narrowband definition.

The spectral narrowband definition is based purely on the bandwidth of the signal as compared to the center frequency. This definition uses the *fractional bandwidth* metric defined as

$$\%BW = \frac{B}{f_{\text{cent}}} \quad (18)$$

where  $B$  is the bandwidth of the emission. The signal is assumed to be narrowband if the fractional bandwidth is below some predefined threshold (10% is typically used).

The array narrowband definition is based on the array geometry and the bandwidth of the signal as

$$B \cdot \Delta\tau_{\text{max}} \ll 1. \quad (19)$$

This relationship allows for the time delay between elements to be treated as a phase shift. When the product in (19) approaches 1, the true-time difference between elements must be considered. Inserting (16) into (19) yields

$$B \cdot \frac{M-1}{2f_d} \ll 1, \quad (20)$$

which can be rewritten in terms of fractional bandwidth as

$$\%BW \cdot \frac{(M-1)}{2f_d/f_{\text{cent}}} \ll 1. \quad (21)$$

The number of array elements  $M$ , the frequency ratio  $f_d/f_{\text{cent}}$  and the fractional bandwidth  $\%BW$  are the three relative parameters that fully characterize a wideband ULA.

### D. Invisible space

As stated in Section II, the invisible domain resides beyond end-fire (in terms of electrical angle) for a uniform linear array and contains the well-known grating lobe series [28]. The invisible space does not correspond to a physical direction and can be represented as complex spatial angles ( $|\sin \theta| > 1$ ). For now, consider a narrowband array. Fig. 3 shows the visible and invisible regions for the grating lobe series for a center-steered,  $M = 30$  element narrowband array with half wavelength spacing that equates to the ratio  $f/f_d = 1$ .

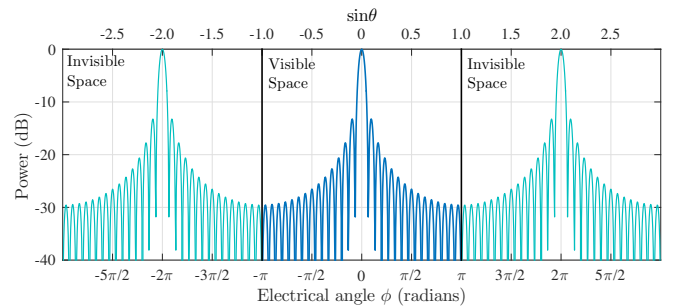


Fig. 3. Visible and invisible regions for an  $M = 30$  element narrowband array with  $f/f_d = 1$ . Not possible to place energy into invisible space.

The feasible array excitations point to electrical angles  $\phi \in [-\pi, \pi]$  due to wrapping of the phase beyond these values. For  $f/f_d = 1$ , these electrical angles perfectly fill the visible

region ( $|\sin \theta| \leq 1$ ). Therefore, if the main beam is steered into the invisible space, it will be “replaced” by a grating lobe entering the visible space from the opposite endfire direction.

In contrast, Fig. 4 shows the visible and invisible regions for the same  $M = 30$  element array but with quarter-wavelength spacing ( $f/f_d = 0.5$ ). The array spacing has now shrunk the visible space to the range of electrical angle values  $|\phi| \leq \pi/2$ . Array excitations that emit a majority of the transmitted energy into the directions  $\pi/2 < |\phi| \leq \pi$  (the red portion in Fig. 4) are associated with large amounts of reactive power, potentially corresponding to power reflections if not properly matched. This region is referred to as the *reactive region*.

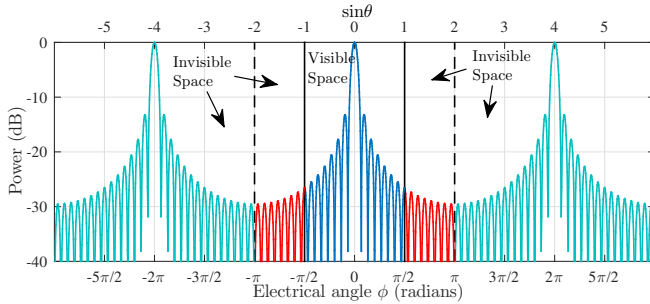


Fig. 4. Visible and invisible regions for an  $M = 30$  element narrowband array with  $f/f_d = 0.5$ . Red portion represents reactive region.

For a wideband scenario, the electrical spacing between antenna elements cannot be assumed to be constant over the bandwidth of the emission. Fig. 5 shows how the ratio of invisible space to visible space changes as the normalized frequency  $f/f_d$  is varied.

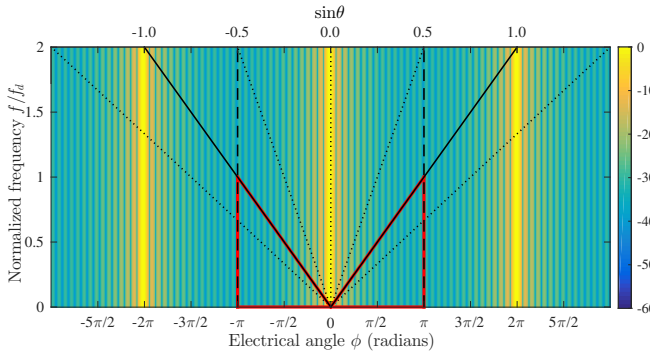


Fig. 5. Visible and invisible regions for an  $M = 30$  element narrowband array with variable  $f/f_d$ . The reactive region is bounded inside the red triangles.

The frequency  $f$  in Fig. 5 is varied from 0 to  $2f_d$  on the vertical axis. The diagonal traces correspond to particular values of  $\sin \theta$ . The vertical dashed lines signify the points at which the electrical angle is  $\phi = \pm\pi$  just as in Figs. 3 and 4. The frequency  $f = f_d$  is the point at which the vertical dashed lines intersect the diagonal solid black lines (corresponding to  $\sin \theta = \pm 1$ ). The area bounded in red is the reactive region as described in Fig. 4 for frequencies less than  $f_d$ . This bounded area is generally not a problem for narrowband systems. However, the reactive region can become a problem when steering towards endfire or for wide beam (standard

or MIMO) emissions without consideration of the frequency-dependent beam pattern, for which energy could unknowingly be placed in the reactive region.

Since the energy stored in the invisible space does not get emitted into the far-field, an emission efficiency metric can be calculated. Define the fractional reactive power (FRP) as the ratio of average reactive power contained in the invisible domain to average power of the total emission as

$$\text{FRP} = \frac{\int_0^{f_d} \left[ \int_{-\pi}^{-\pi f/f_d} |g(f, \phi)|^2 d\phi + \int_{\pi f/f_d}^{\pi} |g(f, \phi)|^2 d\phi \right] df}{\int_0^{\infty} \int_{-\pi}^{\pi} |g(f, \phi)|^2 d\phi df} \times 100\%. \quad (22)$$

The formulation in (22) is based on the assumption that the energy contained within the invisible space accounts for all of the reactive power in the emission, and that the energy contained within the visible space is fully emitted (no reflected power). This efficiency definition does not account for ohmic losses or reflections due to scan impedance variation within the visible space [28], [29].

For example, consider a discretized waveform matrix  $\mathbf{S}$  used to produce a wideband MIMO emission having a fractional bandwidth  $\% \text{BW} = 40\%$  and an omnidirectional beam pattern (in terms of average power) without consideration of the reactive region. The array is comprised of  $M = 30$  equispaced elements with inter-element spacing according to (3) with  $f_d = 1.2f_{\text{cent}}$  which sets the element spacing according to the highest frequency within the bandwidth; a common practice to prevent grating lobes from appearing in-band [34].

Fig. 6 shows the frequency content of the described emission versus electrical angle  $\phi(f, \theta)$  and normalized frequency  $f/f_{\text{cent}}$ . Note the intersection points of  $\sin \theta = \pm 1$  and  $\phi = \pm 1$  occurs at frequency  $f_d$ . The reactive region is again bounded by the red triangles. Using (22), the FRP for this scenario comprises 17.4% of the total average power in the emission. This scenario shows the need to consider the invisible space for wideband emission design when a portion of the bandwidth has an electrical antenna spacing less than a half-wavelength.

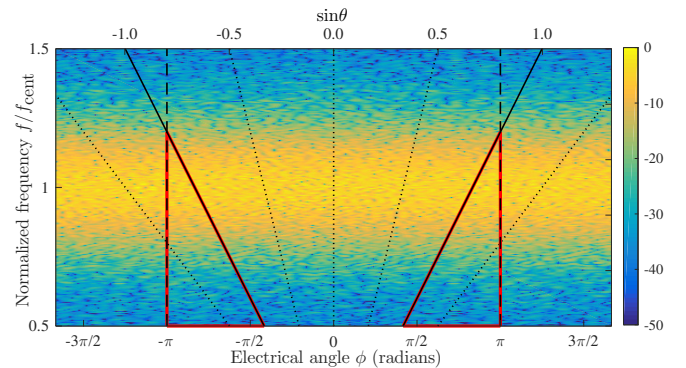


Fig. 6. Spectrum of wideband ( $\% \text{BW} = 40\%$  bandwidth) omnidirectional MIMO emission versus electrical angle  $\phi(f, \theta)$  for an  $M = 30$  element ULA with  $f_d = 1.2f_{\text{cent}}$ . The reactive region is bounded inside the red triangles and comprises 17.4% of the total average power.

The power in the reactive region can be minimized by either 1) increasing the spacing between antenna elements such that

no portion of the bandwidth has an electrical spacing below half-wavelength or 2) constraining the emitted energy to the visible space either by design or traditional beamforming. The first method, while valid, does not prevent grating lobes from appearing [36]. Thus we shall consider how to design of the emission spectral content in the visible space as a means to minimize the power in the reactive region.

#### IV. WIDEBAND MIMO EMISSION OPTIMIZATION WITH SPACE-FREQUENCY NULLING

The proposed design method was first presented in [12] and extended here to also include space-frequency nulling to address spectral coexistence issues [37], [38]. The algorithm is a space-frequency generalization of the approach used in [20] where a non-recurrent form of frequency-modulated continuous wave (FMCW) radar was developed and experimentally demonstrated. That same previous approach was also used in [21] to perform joint FM waveform/taper optimization yielding an ultra-low sidelobe emission that was experimentally demonstrated to achieve a peak sidelobe level (PSL) of  $-83$  dB with only 0.26 dB of SNR loss. In general, this manner of optimization falls within the class of alternating projection approaches, such as [14]–[19].

Here the emitted wideband spectrum is shaped in certain pre-defined angles denoted as “beamlets”, where each beamlet has a specific spectral window (e.g. Gaussian) with predefined 98% bandwidth. For a length  $M$  uniform linear array the  $M$  waveforms are constrained to have constant amplitude, with the discretized version used for optimization being oversampled to account for spectral roll-off and to facilitate sufficient fidelity for subsequent continuous implementation. The space-frequency nulling is performed using the Reiterative Uniform-Weight Optimization (RUWO) algorithm which iteratively enforces nulls given interference matrix  $\mathbf{R}$  while maintaining constant amplitude vectors [22]. Note that the two iterative loops are nested: the outer loop is the spectral/beam pattern shaping design and the inner loop is the RUWO nulling.

##### A. Parameter initialization

1) *Beamlet steering vectors*: Let the uniform linear array have element spacing  $d$  as defined in (3). The sampling frequency is  $f_{\text{samp}} = \gamma B$ , where  $\gamma$  is a scalar over-sampling factor and  $B$  is the 98% bandwidth. It has been found that  $\gamma = 3$  tends to provide sufficient over-sampling to adequately approximate a continuous-time waveform. The discrete length of the waveform defined in (15) can thus be written as  $N = \gamma BT$ , where  $BT$  is the time-bandwidth product.

Denote  $\Theta_P = \{\theta_0, \dots, \theta_{P-1}\}$  as the set containing the  $P$  beamlets to be included in the design. From (5), (12) and (13), the  $p$ th beamlet spatial angle  $\theta_p$  corresponds to the discretized frequency-dependent electrical angles

$$\phi(f_q, \theta_p) = \pi \frac{\left( f_{\text{samp}} \left( -\frac{1}{2} + \frac{q}{Q} \right) + f_{\text{cent}} \right)}{f_d} \sin \theta_p, \quad (23)$$

for  $q = 0, 1, \dots, Q - 1$  over the set of  $p = 0, 1, \dots, P - 1$  beamlets. Note that the number of frequency points  $Q$  must meet the condition of (17) to account for sample shifts that

occur in true time delay processing of wideband emissions. Inserting  $f_{\text{samp}} = \gamma B$  into (23) and dividing the numerator and denominator by  $f_{\text{cent}}$  yields

$$\phi(f_q, \theta_p) = \pi \frac{\left( \%BW \times \gamma \left( -\frac{1}{2} + \frac{q}{Q} \right) + 1 \right)}{f_d/f_{\text{cent}}} \sin \theta_p, \quad (24)$$

which can be readily inserted into (10) to form the steering vectors  $\mathbf{v}(f_q, \theta_p)$  that correspond to the  $P$  beamlets and subsequently the space-frequency steering vectors  $\mathbf{t}(f_q, \theta_p)$  using (9). The formulation in (24) allows for direct implementation of the fractional bandwidth  $\%BW$  and the ratio  $f_d/f_{\text{cent}}$  which sets the intersection points of  $\sin \theta = \pm 1$  and  $\phi = \pm \pi$  as described in Figs. 5 and 6. Define

$$\mathbf{T}(\theta_p) = \left[ \mathbf{t}(f_0, \theta_p) \quad \dots \quad \mathbf{t}(f_{Q-1}, \theta_p) \right] \quad (25)$$

as the  $MN \times Q$  transformation matrix that steers towards spatial angle  $\theta_p$  and performs a discrete Fourier transform.

2) *Spectral windows and adaptive beamlet weighting*: Each of the  $P$  beamlets is shaped according to a desired spectral window. Define the  $Q \times 1$  (magnitude) spectral window for the  $p$ th beamlet as

$$\mathbf{u}(\theta_p) = \left[ u(f_0, \theta_p) \quad \dots \quad u(f_{Q-1}, \theta_p) \right]^T \quad (26)$$

is scaled for a desired amount of power for the corresponding beamlet. For simplicity we shall assume that the  $P$  spectral windows are identical, though the beamlets can have non-identical spectral windows<sup>1</sup>. Note that the spectral window extends over the frequency interval  $f_{\text{cent}} \pm f_{\text{samp}}/2$ , such that the 98% bandwidth is contained in  $1/\gamma$  of the total spectral window centered at  $f_{\text{cent}}$ .

Depending on the number of antenna elements, the  $P$  beamlets will likely be correlated to some extent. Therefore the relative scaling of the spectral windows  $\mathbf{u}(\theta_p)$  must be adapted to prevent the design process from overemphasizing (or underemphasizing) a given beamlet, thus ensuring that the desired beam pattern is formed. Define  $b(\theta_p)$  as the adaptive scaling that dictates the relative contributions of the  $p$ th beamlet so as to achieve the desired joint spectrum/beam pattern set when constructing  $\mathbf{u}(\theta_p)$  for  $p = 0, \dots, P - 1$ . Therefore the spectral window including the adaptive weighting is  $b(\theta_p)\mathbf{u}(\theta_p)$ . Computation of this adaptive scaling is defined in Section IV-B.

3) *Interference covariance matrix*: Define  $L$  space-frequency points to be nulled  $(f_\ell, \theta_\ell)$  for  $\ell = 0, 1, \dots, L - 1$ . Denote  $\Theta_L = \{\theta_0, \dots, \theta_{L-1}\}$  and  $\mathbf{f}_L = \{f_0, \dots, f_{L-1}\}$  as the sets containing the spatial angles and corresponding frequencies to be nulled. These points can be condensed into a region to achieve a broad null or can be placed individually. Collect the corresponding space-frequency steering vectors into the  $MN \times L$  nulling matrix

$$\mathbf{D} = \left[ \mathbf{t}(f_0, \theta_0) \quad \mathbf{t}(f_1, \theta_1) \quad \dots \quad \mathbf{t}(f_{L-1}, \theta_{L-1}) \right]. \quad (27)$$

<sup>1</sup>The same spectral shape should be used when approximating a wide beam using multiple beamlets.

Thus the  $NM \times NM$  wideband space-frequency interference matrix can be defined as

$$\mathbf{R} = \frac{1}{L} \mathbf{D} \mathbf{D}^H + \eta \mathbf{I}_{NM} \quad (28)$$

where  $\eta$  is a loading factor and  $\mathbf{I}_{NM}$  is the  $NM \times NM$  identity matrix. The loading factor  $\eta$  supplements the rank of the interference matrix so that it can be inverted. If the loading factor is too large, the depth of the null will decrease due to the loading factor masking essential eigenvalues. After inversion it is advantageous to normalize  $\mathbf{R}^{-1}$  such that the maximum eigenvalue is unity (the maximum eigenvalue before normalization is approximately  $\eta^{-1}$ ) so that a product with the matrix is neither amplified nor attenuated.

If the space-frequency null locations defined by the sets  $\Theta_L$  and  $\mathbf{f}_L$  coincide with a value in  $u(f_q, \theta_p)$ , for  $p = 0, 1, \dots, P-1$  and  $q = 0, 1, \dots, Q-1$ , then the spectral window must also be nulled accordingly to prevent the design process from filling in the null when shaping the spectrum. Note that nulling within a spectral window necessitates additional scaling to achieve the desired power within the beam containing the null.

4) *Waveform initialization*: Because this emission design scheme allocates power jointly in space-frequency, the process does not directly minimize cross-correlation of the fast-time far-field emission as a function of spatial angle. However, to the degree to which the desired space/frequency response is similar to the initialization, low cross-correlation can be retained if present in the initial emission structure (e.g. see cross-correlation results for optimized emission cases in Section VI). Of course, the presence of space-frequency nulls limits the available degrees of freedom (see [39]) and thus can be expected to increase cross-correlation. It should also be noted that the structure of the  $M$  waveforms is only important insofar as they are amenable to the radar transmitter (constant amplitude, well-contained spectrally) and realize the desired far-field emission within the physical constraints of the array.

### B. Emission design via alternating projections

The beampattern matching design problem for beamlet directions  $\Theta_P$ , with space-frequency nulling defined in  $\Theta_L$  and  $\mathbf{f}_L$ , can be expressed as

$$\begin{aligned} & \underset{\mathbf{s}}{\text{minimize}} && \sum_{p=0}^{P-1} \left\| \frac{1}{M} \mathbf{T}^H(\theta_p) \mathbf{s} - \mathbf{u}(\theta_p) \right\|^2 \\ & \text{subject to} && |s_n^m| = 1, \quad n = 0, \dots, N-1, m = 0, \dots, M-1 \\ & && \mathbf{D}^H \mathbf{s} = \mathbf{0}_{L \times 1} \\ & && |\sin \Theta_P| \leq 1 - \frac{2f_d/f_{\text{cent}}}{M \left(1 - \frac{\% \text{BW}}{2}\right)} \end{aligned} \quad (29)$$

where  $\mathbf{s}$  is the vectorized form of the discretized waveform matrix  $\mathbf{S}$ ,  $s_n^m$  is the  $n$ th time sample of the  $m$ th waveform,  $\|\bullet\|^2$  is the squared-Euclidean norm,  $|\bullet|$  takes the absolute value, and  $\mathbf{0}_{L \times 1}$  is an  $L \times 1$  vector of zeros. The consequence of requiring constant modulus waveforms is that this design

problem is non-convex and must be solved in an iterative manner.

The third constraint in (29) limits the available beamlet directions in  $\Theta_P$  such that the entire mainlobe of each is within the visible region according to the lowest frequency (widest spatial beamwidth). This constraint is established in Appendix A.

Given the initializations from Section IV-A, the  $Q \times 1$  frequency vector of the  $p$ th beamlet at the  $i$ th iteration can be expressed as

$$\mathbf{g}_i(\theta_p) = \frac{1}{M} \mathbf{T}^H(\theta_p) \mathbf{s}_i \quad (30)$$

which is in the cost function in (29). It is implicit assumed that the relative scaling between  $\mathbf{u}(\theta_p)$  and  $\mathbf{g}_i(\theta_p)$  is such that they can be directly compared. However, it has been found that this relationship tends to not occur due to the constant amplitude constraint. Thus, a normalized emission design cost function can be defined as

$$J(i) = \sum_{p=0}^{P-1} \left\| \frac{|\mathbf{g}_i(\theta_p)|}{\sqrt{\gamma_{g,i}}} - \frac{\mathbf{u}(\theta_p)}{\sqrt{\gamma_u}} \right\|^2, \quad (31)$$

where

$$\gamma_{g,i} = \sum_{p=0}^{P-1} \|\mathbf{g}_i(\theta_p)\|^2 \quad (32)$$

and

$$\gamma_u = \sum_{p=0}^{P-1} \|\mathbf{u}(\theta_p)\|^2 \quad (33)$$

are the total powers contained in the beamlets of the current iteration  $i$  and the predefined spectral windows, respectively. The formulation in (31) compares the relative difference rather than the absolute difference to prevent artificially increasing cost due to scaling.

Using (30), the adaptive scaling for the  $p$ th beamlet is updated as

$$b_{i+1}(\theta_p) = b_i(\theta_p) \sqrt{\frac{\|\mathbf{u}(\theta_p)\|^2 / \gamma_u}{\|\mathbf{g}_i(\theta_p)\|^2 / \gamma_{g,i}}}. \quad (34)$$

As the iterative design progresses the term inside the  $\sqrt{\bullet}$  converges to unity, thus producing a beam scaling value  $b(\theta_p)$  that produces the desired spatial beam power specified in  $\mathbf{u}(\theta_p)$ .

The spectral window and beam scaling for the  $p$ th beam is applied as

$$\tilde{\mathbf{g}}_i(\theta_p) = b_{i+1}(\theta_p) [\mathbf{u}(\theta_p) \odot \exp(j \angle \mathbf{g}_i(\theta_p))], \quad (35)$$

where  $\odot$  is the Hadamard product and  $\angle$  extracts the phase angle of the argument (each element in the vector). The unconstrained (in amplitude) vectorized waveform set at the  $i$ th iteration can then be found as

$$\tilde{\mathbf{s}}_i = \sum_{p=0}^{P-1} \mathbf{T}(\theta_p) \tilde{\mathbf{g}}_i(\theta_p), \quad (36)$$

which is equivalent to projecting each beamlet back onto the array, taking the inverse Fourier transform, and summing the  $P$  responses.

If space-frequency nulling is required, denote the current RUWO iteration as  $k$  and the total number of iterations  $K$ . The RUWO loop is initialized using the current estimate of the unconstrained waveforms as  $\mathbf{r}_0 = \exp(j\angle\tilde{\mathbf{s}}_i)$ . The update of the nulled, vectorized waveform set is defined as [22]

$$\mathbf{r}_{k+1} = \exp(j\angle(\mathbf{R}^{-1}\mathbf{r}_k)) \quad (37)$$

where  $\mathbf{R}^{-1}$  is the inverse of the interference covariance matrix from (28). The RUWO cost function is

$$H(k) = \|\mathbf{r}_{k+1} - \mathbf{R}^{-1}\mathbf{r}_k\|^2, \quad (38)$$

where the normalization of  $\mathbf{R}^{-1}$  by the maximum eigenvalue as discussed in Section IV-A causes the terms  $\mathbf{r}_{k+1}$  and  $\mathbf{R}^{-1}\mathbf{r}_k$  to possess comparable amplitudes. The RUWO algorithm is not guaranteed to converge onto a solution that produces the desired nulls, though it has been proven that the cost function in (38) reduces at each iteration  $k$ , thus establishing that it does not diverge [22], [40], [41]. The convergence speed of RUWO is dependent on the rank of interference covariance matrix  $\mathbf{R}$ , but typically converges to a stable solution within  $K = 50$  iterations [22].

The vectorized waveform set is then updated as

$$\mathbf{s}_{i+1} = \begin{cases} \mathbf{r}_K, & \text{when nulling} \\ \exp(j\angle\tilde{\mathbf{s}}_i), & \text{otherwise} \end{cases}. \quad (39)$$

The process (30), (34)–(37), and (39) is repeated a predefined number of times  $\Phi$ . Table I provides a summary of the optimization steps. If nulling is being applied, the per iteration computational cost is dominated by the RUWO loop and is  $O(K(NM)^2)$  in complexity. If no nulling is applied ( $K = 0$ ), then the cost is  $O(PQNM)$  in complexity.

When the nulling stage is removed, it can be shown that this approach can be put into the *Error Reduction Algorithm* (ERA) structures of [19], specifically in the form in Algorithm 6 therein<sup>2</sup>. However, due to the practical issues of 1) needing to avoid the edges of the spatial domain to limit the FRP of the emission (the final constraint in (29)) and 2) needing sufficient time sampling to account for true time delay (17), these forms cannot be solved because the associated matrix is neither unitary nor invertible. Thus, the proposed algorithm deviates from the error reduction form of ERA [18], [19], and therefore cannot be proven analytically to decrease each iteration. However, myriad different simulation scenarios have all been observed to converge to meaningful solutions. Further, the combination of the first and third constraints of (29) with the implementation scheme described in Section V does ensure the result is a physically realizable emission, regardless of how close to optimal it actually is.

<sup>2</sup>The formulation in [19] considers unitary transformation matrices, though non-unitary matrices may also be considered by means of a matrix inverse.

TABLE I  
IMPLEMENTATION OF WIDEBAND MIMO EMISSION DESIGN WITH  
SPACE-FREQUENCY NULLING

1.	Establish the number of antenna elements $M$ and discretized waveform length $N$ for oversampling factor $\gamma$ and time-bandwidth product $BT$ .
2.	Select quantity $P$ and specific directions $\Theta_P$ of the beamlets, the number of frequency bins $Q$ , percent bandwidth %BW, and the ratio $f_d/f_{\text{cent}}$ that dictates element spacing.
3.	Determine the $L$ space-frequency points $\Theta_L$ and $\mathbf{f}_L$ to be nulled (if any). Form the $NM \times NM$ interference matrix $\mathbf{R}$ using (28), calculate the inverse, and normalize by the maximum eigenvalue. Select the number of RUWO iterations $K$ .
4.	Form the spectral shaping vector $\mathbf{u}(\theta_p)$ for each of the $P$ beamlets. Zero values $u(f_q, \theta_p)$ if they contradict with a nulled region.
5.	Set the number of optimization iterations to perform $\Phi$ . Initialize vectorized waveform set $\mathbf{s}_0$ , loop index to $i = 0$ , and the adaptive scaling coefficients $b_0(\theta_p)$ to unity.
6.	Form $\mathbf{g}_i(\theta_p)$ and update $b_{i+1}(\theta_p)$ for $p = 0, \dots, P-1$ via (30) and (34).
7.	Apply beamscale $b_{i+1}(\theta_p)$ and spectral shaping using $\mathbf{u}(\theta_p)$ to form $\tilde{\mathbf{g}}_i(\theta_p)$ for $p = 0, \dots, P-1$ via (35).
8.	Form the unconstrained vectorized waveform set $\tilde{\mathbf{s}}_i$ via (36).
9.	If no nulling is being applied, set $\mathbf{s}_{i+1} = \exp(j\angle\tilde{\mathbf{s}}_i)$ and go to step 11.
10.	Initiate RUWO nulling loop. Set loop index to $k = 0$ .
a.	Form initial vectorized solution $\mathbf{r}_0 = \exp(j\angle\tilde{\mathbf{s}}_i)$ .
b.	Update vectorized solution $\mathbf{r}_{k+1}$ using (37).
c.	Increment $k = k + 1$ . Stop if $k = K$ . Otherwise, and go to step 10b.
d.	Set $\mathbf{s}_{i+1} = \mathbf{r}_K$ .
11.	Increment $i = i + 1$ . If $i = \Phi$ , go to step 12. Otherwise, go to step 6.
12.	Implement discretized waveform set $\mathbf{s}_\Phi$ as physically realizable FM waveforms as shown in Sect. V.

## V. IMPLEMENTATION

The constant modulus, discrete-time, baseband representation of the optimized waveform set  $\mathbf{s}_\Phi$  can be translated into  $M$  continuous-time waveforms using the polyphase-coded FM (PCFM) implementation [13].

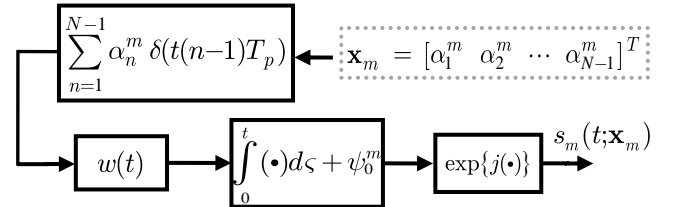


Fig. 7. Implementation of  $m$ th polyphase-coded frequency-modulated (PCFM) waveform

Given the length- $N$  phase sequence of the  $m$ th discretized waveform  $\psi_0^m, \psi_1^m, \dots, \psi_{N-1}^m$ , for  $\psi_n^m = \angle s_n^m$ , a train of  $N-1$  impulses with time separation  $T_p = 1/f_{\text{samp}}$  are formed. The  $n$ th impulse is weighted by  $\alpha_n^m$ , which is equal to the modulo phase change between the  $n$ th and  $(n-1)$ th phase value as determined by

$$\alpha_n^m = \begin{cases} \tilde{\alpha}_n^m & \text{if } |\tilde{\alpha}_n^m| \leq \pi \\ \tilde{\alpha}_n^m - 2\pi\text{sgn}(\tilde{\alpha}_n^m) & \text{if } |\tilde{\alpha}_n^m| > \pi \end{cases} \quad (40)$$

where

$$\tilde{\alpha}_n^m = \psi_n^m - \psi_{n-1}^m \quad \text{for } n = 1, \dots, N-1 \quad (41)$$

and  $\text{sgn}(\bullet)$  is the sign function.

The values of (40) can then be collected into the phase-change sequence  $\mathbf{x}_m = [\alpha_1^m \ \alpha_2^m \ \dots \ \alpha_{N-1}^m]^T$  that parameterizes the  $m$ th complex-baseband waveform. The pulse train is then convolved with a shaping filter  $w(t)$  that has a time duration of  $T_p$  and integrates to unity over the real line (e.g. a rectangular pulse or a raised cosine). The continuous phase function is then found through a cumulative integration with respect to the time dummy variable  $\varsigma$ , with initial phase  $\psi_0^m$  as seen in Fig. 7. The resulting  $m$ th complex-baseband, constant-amplitude, continuous FM waveform is

$$s_m(t; \mathbf{x}_m) = \exp \left\{ j \left( \int_0^t w(\varsigma) * \left[ \sum_{n=1}^{N-1} \alpha_n^m \delta(\varsigma - (n-1)T_p) \right] d\varsigma + \psi_0^m \right) \right\}. \quad (42)$$

Note that the inherent filtering (by shaping filter  $w(t)$ ) involved in the PCFM implementation may slightly alter the spectrum in lower power areas of the frequency response. Thus the nulls that have been enforced in the optimization may “fill in” to some degree. The loss in null sensitivity can be mitigated by applying the design process at a higher sampling rate [42].

## VI. EMISSION OPTIMIZATION ANALYSIS

Consider the design of a wideband emission having time-bandwidth product  $BT = 50$  and fractional bandwidth  $\%BW = 40\%$  for a uniform linear array comprised of  $M = 30$  antenna elements. The antenna element spacing is set according to the highest frequency in bandwidth  $B$  to reduce the effect of grating lobes [34]. The normalized frequency associated with this spacing is

$$\frac{f_d}{f_{\text{cent}}} = \frac{f_{\text{cent}} + B/2}{f_{\text{cent}}} = 1 + \frac{\%BW}{2} = 1.2. \quad (43)$$

The sampling frequency is set to  $\gamma = 5$  times the time-bandwidth product of  $BT = 50$  (so  $N = 5(50) = 250$ ) to closely approximate a continuous-time waveform. The maximum sample delay occurring for true-time delay processing is

$$f_{\text{samp}} \cdot \Delta\tau_{\text{max}} = \gamma(M-1) \frac{\%BW}{2f_d/f_{\text{cent}}} = 23.2 \text{ samples}. \quad (44)$$

Therefore from (17), the minimum number of frequency samples needed is  $250 + \lceil 23.2 \rceil = 274$  to prevent aliasing of the complex envelope. As stated in Section III-B, the Gibbs phenomenon produces time sidelobes beyond the extent of the pulsewidth [35], and thus  $Q = 2N = 500$  frequency points are used to minimize this effect.

For the given array, the set of beamlets must be contained within the spatial region established by the third constraint of (29) as

$$|\sin \Theta_P| \leq 1 - \frac{2f_d/f_{\text{cent}}}{M \left( 1 - \frac{\%BW}{2} \right)} = 0.9 \quad (45)$$

to avoid placing appreciable power in the reactive region.

Using these parameters as a baseline, three different scenarios are simulated and analyzed to highlight the customizable design capabilities that are possible. In Case 1)  $P = 3$  beamlets are chosen to point in the directions  $\sin \Theta_P \in \{-0.71, 0, 0.17\}$ . The  $\sin \theta = 0$  beam is set to have 3 dB higher power than the other two beams and has a wide space-frequency null bounded by normalized frequencies  $\mathbf{f}_L \in [1.2, 1.4]$  and angles  $\sin \Theta_L \in [0.10, 0.25]$ . For Case 2) a wide (nearly omnidirectional) beam is generated over the angular interval  $\sin \Theta_P \in [-0.9, 0.9]$ , which is realized using  $P = 60$  evenly spaced beamlets. Power is distributed equally over this wide beam and two nulled regions are included that are bounded by normalized frequencies  $\mathbf{f}_L \in \{[0.8, 0.9], [1.2, 1.4]\}$  with corresponding angle intervals  $\sin \Theta_L \in \{[-0.5, -0.42], [0.10, 0.25]\}$ . Finally, for Case 3) a moderately wide beam and a narrow secondary beam are jointly optimized over  $\sin \Theta_P \in \{[-0.5, 0.5], 0.75\}$ . The wide beam is generated using 30 evenly spaced beamlets over the interval, thus making for a total of  $P = 31$  beamlets. The secondary beam pointed in the direction  $\sin \theta = 0.75$  is set to be 2 dB higher than the peak power of the wide beam. The wide beam is specified to have a Gaussian-tapered spatial power distribution. Case 3 has the same null conditions as Case 2.

All the beamlets are nominally (excluding nulls) designed to have a Gaussian spectral shape in frequency for three reasons: 1) to establish the bandwidth of the emission, 2) to incorporate the spectral roll-off and thus well approximate a continuous-time emission, and 3) to leverage the desirable autocorrelation properties associated with a Gaussian power spectral density [43]. Table II shows a summary of the frequency, beamlet, and null constraints for each case.

TABLE II  
SUMMARY OF FREQUENCY, BEAMLET AND NULL CONSTRAINTS

	Case 1	Case 2	Case 3
$Q$	500	500	500
Spectral shape	Gaussian	Gaussian	Gaussian
$P$	3	60	30 + 1
$\sin \Theta_P$	-0.71, 0, 0.17	[-0.9, 0.9]	[-0.5, 0.5] {0.75} <sup>††</sup>
Relative powers	0dB, 3dB, 0dB	Equal	Tapered (peak 0dB) {2dB} <sup>††</sup>
$\sin \Theta_L$	[0.10, 0.25]	[0.10, 0.25] <sup>†</sup> [-0.5, -0.42]	[0.10, 0.25] <sup>††</sup> [-0.5, -0.42]
$\mathbf{f}_L$	[1.2, 1.4]	[1.2, 1.4] <sup>†</sup> [0.8, 0.9]	[1.2, 1.4] <sup>††</sup> [0.8, 0.9]

<sup>†</sup>, <sup>††</sup> denotes specific relationships for parameters with multiple entries

Each case uses  $\Phi = 100$  design iterations along with  $K = 20$  RUWO iterations. These values were selected because it was observed that sufficient convergence was obtained, though more sophisticated stopping criteria could alternatively be employed. Convergence plots are presented for the RUWO cost function  $H(k)$  from (38) and emission design cost func-

tion  $J(i)$  from (31). The three cases are examined both with and without adaptive beamlet scaling  $b(\theta_p)$ . The waveform matrix  $\mathbf{S}$  for each of the 3 cases is independently initialized with white, complex-Gaussian distributed data having unit variance and zero mean so as to start with relatively low cross-correlation for the far-field emissions.

#### A. Wideband radar emission analysis

The far-field emission can be assessed by considering the aggregate beampattern, angle-dependent autocorrelation of the fast-time emission, maximum angular cross-correlation, and the fractional reactive power (FRP) defined in (22). The aggregate beampattern is the time-average of the space-time emission over pulsewidth  $T$ , which displays the amount of power emitted versus transmit spatial angle  $\theta$ . Using the continuous time representation of the waveforms from (42) incorporated into the time/angle dependent emission of (7), the aggregate beampattern can be written as

$$B(\theta) = \frac{1}{T} \int_0^T |g(t, \theta)|^2 dt. \quad (46)$$

The scaling of the aggregate beampattern is relative to a single focused beam, the peak of which would be normalized to 0 dB. Thus the overall emitted power remains constant across all three cases.

To address the correlation properties of the emission, define a wideband, frequency domain version of the angle-delay ambiguity function from [44] as

$$A(\tau, \theta, \beta) = \frac{\left| \int_{-\infty}^{\infty} g(f, \theta) g^*(f, \beta) e^{+j2\pi f \tau} \left[ \sum_m e^{jm\pi \frac{f_d}{f} (\sin \theta - \sin \beta)} \right] df \right|^2}{M \int_{-\infty}^{\infty} g^*(f, \beta) g(f, \beta) df} \quad (47)$$

where  $\beta$  is the receive spatial angle. The angle-dependent autocorrelation shows the delay ambiguity properties of the emission versus spatial angle and is defined as the two-dimensional cut of (47) when  $\beta = \theta$ . The maximum angular cross-correlation is the peak correlation of the emission over delay as a function of transmit angle  $\theta$  and receive angle  $\beta$  and is defined as

$$\max_{\tau} A(\tau, \theta, \beta). \quad (48)$$

#### B. Case 1: Three-beam scenario

Fig. 8 shows the wideband spectrum of Case 1 where  $P = 3$  discrete beams are optimized in the directions  $\sin \Theta_P \in \{-0.71, 0, 0.17\}$ , each with a Gaussian spectral shape and the  $\sin \theta = 0$  beam is designed to have 3 dB higher power than the other two beams. The space-frequency null bounded between  $f/f_{\text{cent}} = 1.2$  and  $f/f_{\text{cent}} = 1.4$  and between  $\sin \theta = 0.1$  and  $\sin \theta = 0.25$  can also be observed in this figure. The FRP for this emission is only 1.88% of the total average power.

Fig. 9 shows the aggregate beampattern after emission optimization (blue). The peaks of the  $\sin \theta = -0.71$  and  $\sin \theta = 0.17$  beams exhibit relative powers of  $-6.25$  dB while that of the  $\sin \theta = 0$  beam is  $-3.23$  dB, which is within 0.02 dB of the 3 dB relative power constraint. The red plot in Fig.

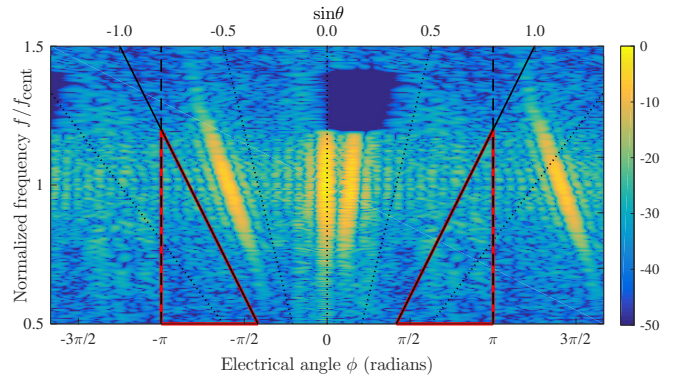


Fig. 8. Spectrum of wideband (%BW = 40% bandwidth) multi-beam MIMO emission versus electrical angle  $\phi(f, \theta)$  for an  $M = 30$  element ULA with  $f_d = f_{\text{cent}} + B/2$ . The reactive region is bounded inside the red triangles and comprises 1.88% of the total average power.

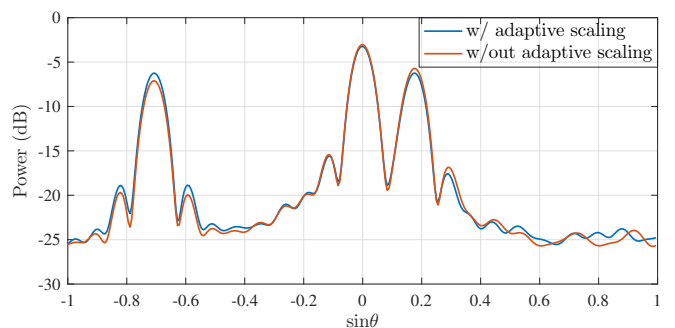


Fig. 9. Aggregate beampattern of wideband (%BW = 40% bandwidth) multi-beam MIMO emission versus  $\sin \theta$  for design with adaptive scaling (blue) and without adaptive scaling (red) for from an  $M = 30$  element ULA with  $f_d = f_{\text{cent}} + B/2$ .

9 represents what the beampattern would look like without the adaptive scaling of the  $P$  beams to enforce the relative power constraint (without which the relative powers between the  $\sin \theta = \{-0.71, 0.17\}$  beams and the center  $\sin \theta = 0$  beam would be 3.4 dB and 2.7 dB respectively instead of the desired 3 dB).

Fig. 10 shows the resulting power spectrum of the three beams and the Gaussian spectral window used in the design

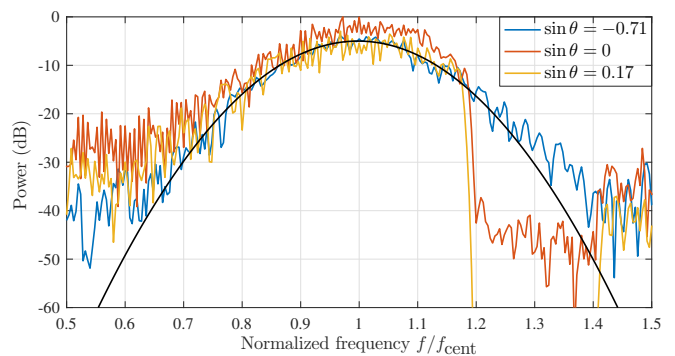


Fig. 10. Emission spectrum for wideband (%BW = 40% bandwidth) multi-beam MIMO emission versus normalized frequency  $f/f_{\text{cent}}$  of the  $P = 3$  beams in the directions  $\sin \theta = -0.71$  (blue),  $\sin \theta = 0$  (red), and  $\sin \theta = 0.17$  (yellow) and the spectral window used for design (black).

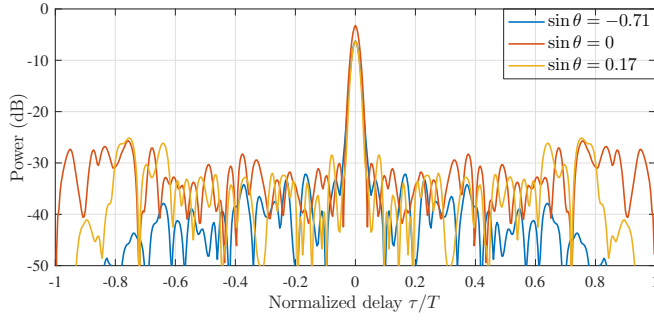


Fig. 11. Autocorrelation function for wideband (%BW = 40% bandwidth) multi-beam MIMO emission of the  $P = 3$  beams in the directions  $\sin \theta = -0.71$  (blue),  $\sin \theta = 0$  (red), and  $\sin \theta = 0.17$  (yellow).

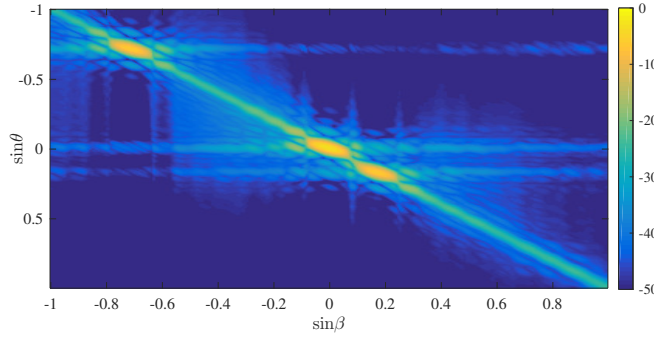


Fig. 12. Maximum angular cross-correlation for wideband (%BW = 40% bandwidth) multi-beam MIMO emission as a function of  $\sin \theta$  and  $\sin \beta$  for an  $M = 30$  element ULA with  $f_d = f_{\text{cent}} + B/2$ .

(shown in black). A scaled version of this Gaussian window was used for the  $\sin \theta = -0.71$  and  $\sin \theta = 0$  beams, while for the  $\sin \theta = 0.17$  beam the impact of the overlapping null region can be observed.

Fig. 11 displays the resulting autocorrelation of the three beams generated via (47) for  $\beta = \theta$ . The peak sidelobe levels relative to their respective mainlobes are  $-26$  dB for  $\sin \theta = -0.71$ ,  $-22.5$  dB for  $\sin \theta = 0$ , and  $-19.45$  dB for  $\sin \theta = 0.17$ . The slight sidelobe increase for the  $\sin \theta = 0.17$  beam is a result of the null in its spectrum.

Fig. 12 depicts the maximum temporal cross-correlation of the emission as a function of transmit ( $\theta$ ) and receive ( $\beta$ ) angles via (48) where the diagonal is the peak autocorrelation. The responses from the three beamlets are clearly shown on the diagonal of the plot. The peak-normalized,  $\tau/T = 0$  cut of the angle-delay ambiguity function versus  $\sin \beta$  for the transmit angles  $\sin \theta = -0.71$ ,  $\sin \theta = 0$ , and  $\sin \theta = 0.17$  is shown in Fig. 13. The desired beam locations are indicated by the black, vertical dashed lines. The peak cross-correlation level and spatial resolution of each beam is dependent on the correlation levels of the emission around that beam. Because widely-separated, individual beams are being designed, the spatial ambiguity level and spatial resolution remain similar to that of a standard coherent beamformed emission.

The emission design cost function  $J(i)$  from (31) is shown in Fig. 14 versus iteration index  $i$  for versions with (blue) and without (red) adaptive scaling. The cost function value converges to a solution after 5 iterations for both scenarios

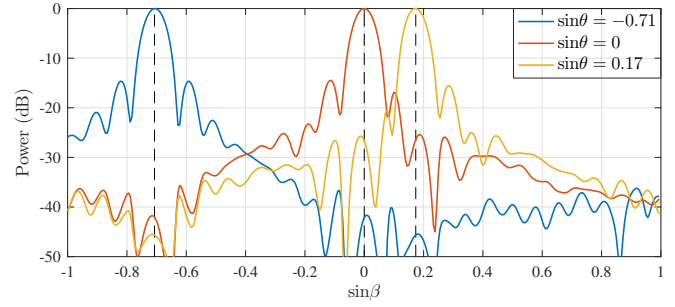


Fig. 13. Peak-normalized angle-delay ambiguity function at  $\tau/T = 0$  for wideband (%BW = 40% bandwidth) multi-beam MIMO emission versus  $\sin \beta$  for the transmit angles  $\sin \theta = -0.71$  (blue),  $\sin \theta = 0$  (red), and  $\sin \theta = 0.17$  (yellow), corresponding to the  $P = 3$  beam directions.

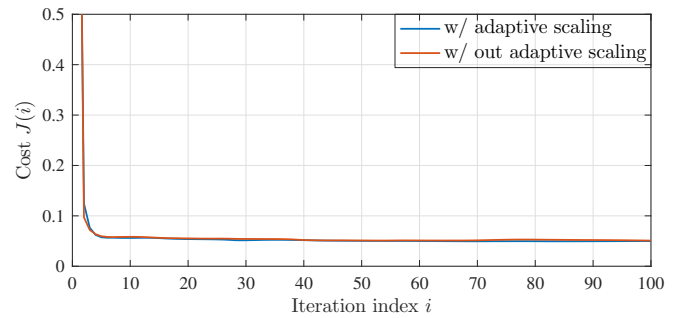


Fig. 14. Emission design cost function  $J(i)$  versus iteration index  $i$  ( $\Phi = 100$  iterations;  $K = 20$  nulling iterations) for wideband (%BW = 40% bandwidth) multi-beam MIMO emission with adaptive scaling (blue) and without adaptive scaling (red) for an  $M = 30$  element ULA with  $f_d = f_{\text{cent}} + B/2$ .

and remains at approximately that level for the remainder of the iterations. The versions with and without the adaptive scaling have similar convergence. Fig. 15 shows the RUWO cost function  $H(k)$  from (38) versus iteration index  $k$  for all  $\Phi = 100$  iterations, where the error reduction property can be observed.

### C. Case 2: Wide-beam scenario

Fig. 16 shows the spectrum for Case 2 where a near-omnidirectional wide beam has been designed to exist between  $\sin \theta = -0.9$  and  $\sin \theta = 0.9$ , where the bound described in

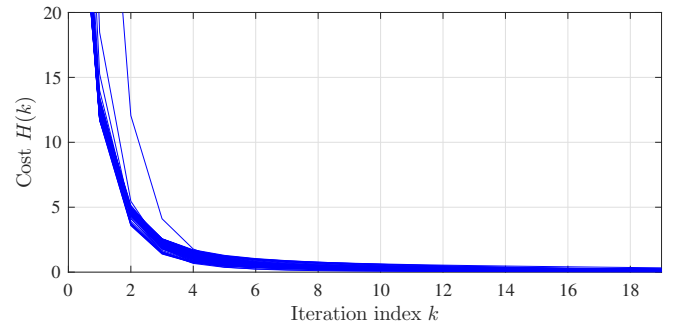


Fig. 15. RUWO cost function  $H(k)$  versus iteration index  $k$  ( $\Phi = 100$  iterations;  $K = 20$  nulling iterations) for wideband (%BW = 40% bandwidth) multi-beam MIMO emission for an  $M = 30$  element ULA with  $f_d = f_{\text{cent}} + B/2$ .

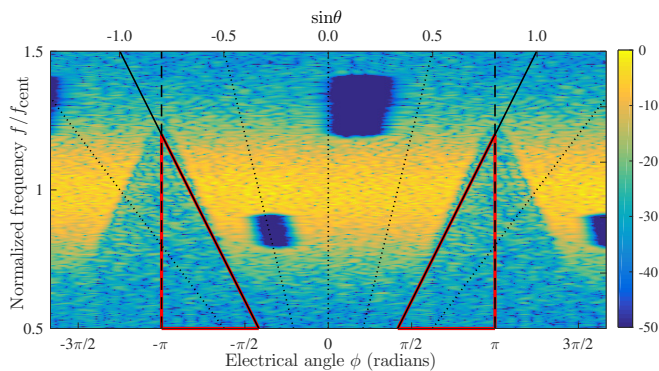


Fig. 16. Spectrum of wideband (%BW = 40% bandwidth) wide beam MIMO emission versus electrical angle  $\phi(f, \theta)$  for an  $M = 30$  element ULA with  $f_d = f_{\text{cent}} + B/2$ . The reactive region is bounded inside the red triangles and comprises 1.35% of the total average power.

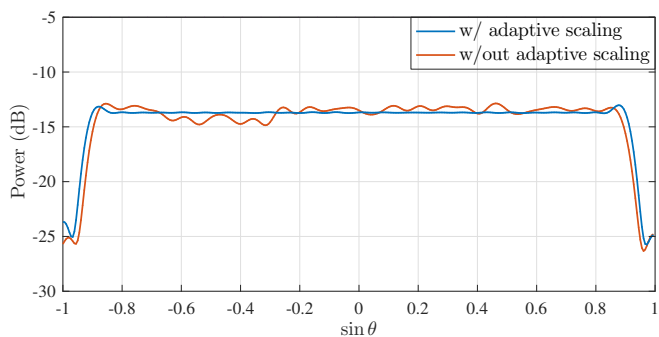


Fig. 17. Aggregate beampattern of wideband (%BW = 40% bandwidth) wide beam MIMO emission versus  $\sin \theta$  for optimization with adaptive scaling (blue) and without adaptive scaling (red) for from an  $M = 30$  element ULA with  $f_d = f_{\text{cent}} + B/2$ .

(45) prevents the mainlobe of each beamlet from residing in the reactive region (bounded in red) for all in-band frequencies. The wide beam is constructed using  $P = 60$  equal-spaced beamlets and shaped to a Gaussian frequency spectrum. The FRP for this case is 1.35% of the total average power, which is a substantial reduction from the 17.4% for the previous near-omnidirectional emission presented in Section III-D.

In addition to the null constraint from the previous case, another null is included that comprises the region bounded between normalized frequencies  $f/f_{\text{cent}} = 0.8$  and  $f/f_{\text{cent}} = 0.9$  and spatial angles  $\sin \theta = -0.5$  and  $\sin \theta = -0.42$ .

The aggregate beampattern of this emission, shown in Fig. 17 as the blue trace, has only 0.74 dB of variation over the optimized spatial region of  $\sin \Theta_P \in [-0.90, 0.90]$ . In contrast, the beampattern optimized without the adaptive scaling, shown as the red trace, has 2 dB of power variation.

The angle-dependent autocorrelation for normalized delays  $\tau/T \in [-0.5, 0.5]$  is shown in Fig. 18. The mainlobe of the autocorrelation from spatial regions  $\sin \theta = -0.6$  to  $\sin \theta = -0.3$  is broadened slightly because the null between  $\sin \theta = -0.5$  and  $\sin \theta = -0.42$  lies entirely within the bandwidth of the emission.

Fig. 19 depicts the maximum angular cross correlation as a function of  $\theta$  and  $\beta$ . The width of the diagonal depends on

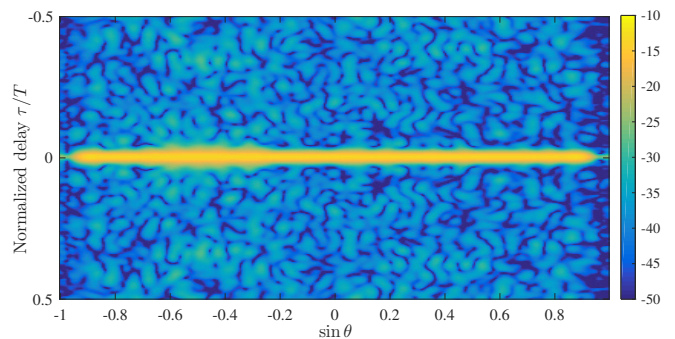


Fig. 18. Autocorrelation function for wideband (%BW = 40% bandwidth) wide beam MIMO emission versus  $\sin \theta$  for normalized delay  $\tau/T \in [-0.5, 0.5]$ .

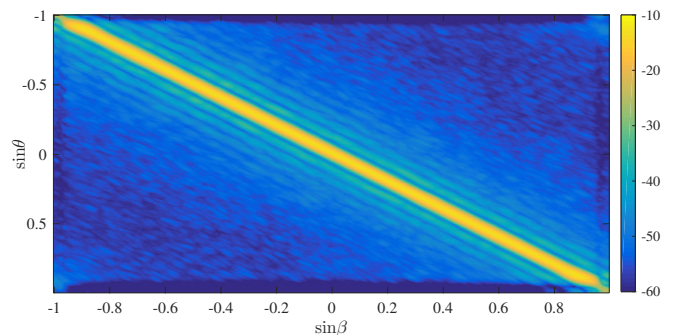


Fig. 19. Maximum angular cross-correlation for wideband (%BW = 40% bandwidth) wide beam MIMO emission as a function of  $\sin \theta$  and  $\sin \beta$  for an  $M = 30$  element ULA with  $f_d = f_{\text{cent}} + B/2$ .

the array size, which dictates the beamwidth and thus limits the level of decorrelation between nearby spatial angles. Fig. 20 shows the peak-normalized angle-delay ambiguity function versus  $\sin \beta$  for the transmit directions  $\sin \theta \in \{-0.9, 0, 0.4\}$  at  $\tau/T = 0$ . Note that both the mainlobe width and cross-correlation level have improved (in terms of resolution and spatial ambiguity) from that in Fig. 13 due to the wide beam design enforcing a stricter spatial decorrelation by including many proximate beamlets ( $P = 60$ ).

The emission design cost function  $J(i)$  is shown in Fig. 21 versus iteration index  $i$  for versions with (blue) and without (red) the adaptive scaling. The scenarios have a similar con-

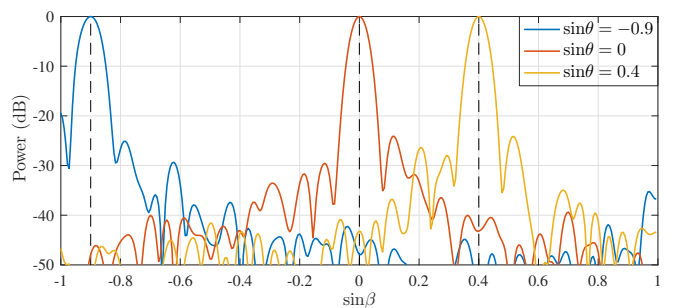


Fig. 20. Peak-normalized angle-delay ambiguity function at  $\tau/T = 0$  for wideband (%BW = 40% bandwidth) wide beam MIMO emission versus  $\sin \beta$  for the transmit angles  $\sin \theta = -0.9$  (blue),  $\sin \theta = 0$  (red), and  $\sin \theta = 0.4$  (yellow).

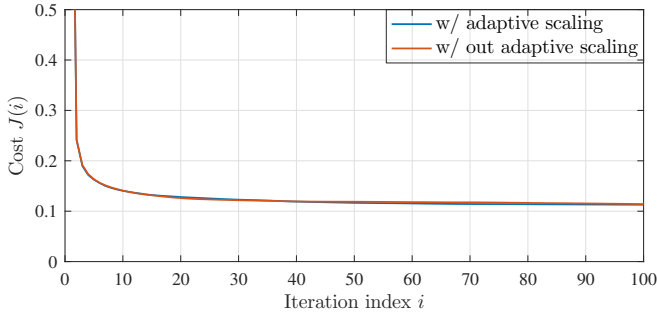


Fig. 21. Emission design cost function  $J(i)$  versus iteration index  $i$  ( $\Phi = 100$  iterations;  $K = 20$  nulling iterations) for wideband (%BW = 40% bandwidth) wide beam MIMO emission with adaptive scaling (blue) and without adaptive scaling (red) for an  $M = 30$  element ULA with  $f_d = f_{\text{cent}} + B/2$ .

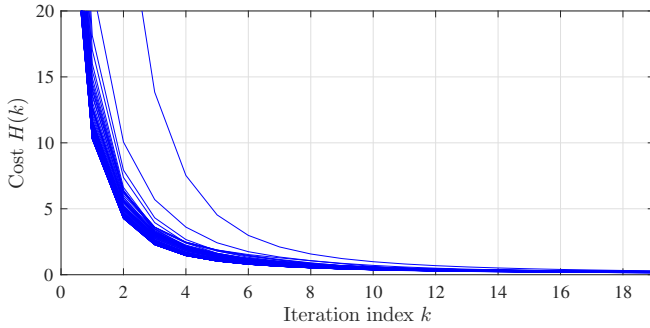


Fig. 22. RUWO cost function  $H(k)$  versus iteration index  $k$  ( $\Phi = 100$  iterations;  $K = 20$  nulling iterations) for wideband (%BW = 40% bandwidth) wide beam MIMO emission for an  $M = 30$  element ULA with  $f_d = f_{\text{cent}} + B/2$ .

vergence behavior, though the scenario with the adaptive beam scaling better constrains the beam pattern of the emission. Fig. 22 shows the RUWO cost function  $H(k)$  versus iteration index  $k$  for all  $\Phi = 100$  iterations. Again the cost function  $H(k)$  decreases at each iteration due to the error reduction property discussed in [22], [40], [41].

#### D. Case 3: Wide beam + secondary beam scenario

Finally, Fig. 23 shows the wideband spectrum for Case 3 where a moderately wide beam is designed to lie between  $\sin \theta = -0.5$  and  $\sin \theta = 0.5$  with a Gaussian spatial taper as well as a narrow secondary beam at  $\sin \theta = 0.75$  that is designed to be 2 dB larger than the peak power of the wide beam. The wide beam was approximated using 30 equally spaced beamlets over the angular region. Including the secondary beam makes a total of  $P = 31$  beamlets for this case. All beams are designed to have a Gaussian spectral shape and the same null constraints as in Case 2. The FRP for this case is found to be 1.74% of the total average power.

The aggregate beam pattern with and without the adaptive scaling is shown in Fig. 24. Due to the close proximity of the beamlets used to construct the wide beam, it is overemphasized relative to the narrow secondary beam when adaptive scaling is omitted (the secondary beam has 5 dB less power than the peak of the wide beam). However, with the adaptive scaling the secondary beam is 2 dB larger than the peak power of the wide beam as originally specified. Also, the shape of the

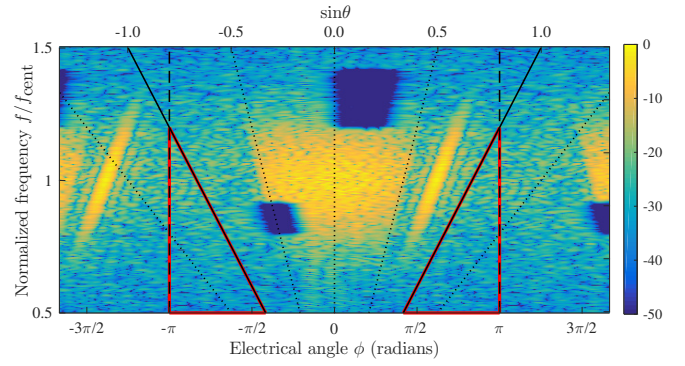


Fig. 23. Spectrum of wideband (%BW = 40% bandwidth) wide beam + secondary beam MIMO emission versus electrical angle  $\phi(f, \theta)$  for an  $M = 30$  element ULA with  $f_d = f_{\text{cent}} + B/2$ . The reactive region is bounded inside the red triangles and comprises 1.74% of the total average power.

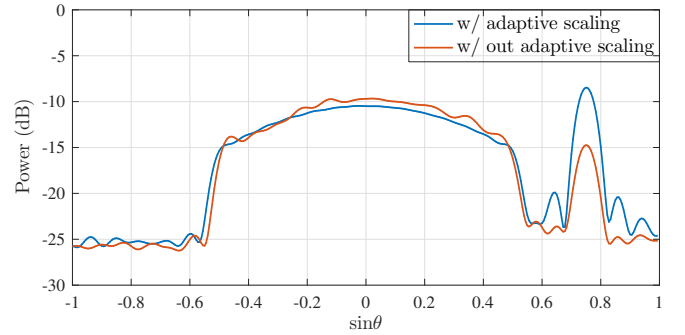


Fig. 24. Aggregate beampattern of wideband (%BW = 40% bandwidth) wide beam + secondary beam MIMO emission versus  $\sin \theta$  for design with adaptive scaling (blue) and without adaptive scaling (red) for an  $M = 30$  element ULA with  $f_d = f_{\text{cent}} + B/2$ .

wide beam better approximates the Gaussian spatial window enforced during the optimization.

The angular autocorrelation for normalized delays  $\tau/T \in [-0.5, 0.5]$  can be seen in Fig. 25. Again, it is observed that the mainlobe of the autocorrelation between  $\sin \theta = -0.6$  and  $\sin \theta = -0.3$  is slightly broadened due to the presence of the null in the bandwidth of the emission in that direction. Also, Fig. 25 shows that the range sidelobes of the narrow secondary beam, on average, are lower than any angle within the wide beam. This difference in sidelobe level arises because the wide beam design involves the conflicting goals of spatial decorrelation and spectral shaping of adjacent beamlets.

The maximum angular cross-correlation is shown in Fig. 26. The peak cross-correlation response is clearly larger in the vicinity of the narrow secondary beam than it is near the widebeam. Expanding on this result, Fig. 27 shows the peak-normalized angle-delay ambiguity function at  $\tau/T = 0$  versus  $\sin \beta$  for the transmit angles  $\sin \theta = \{0, 0.4, 0.75\}$ . Note the difference in ambiguity sidelobe level and shape of the mainlobe for the three directions. The angles  $\sin \theta \in \{0, 0.4\}$  reside within the wide beam and thus have an improved spatial resolution and decreased sidelobe level compared to the secondary beam in  $\sin \theta = 0.75$ , whose resolution and sidelobe

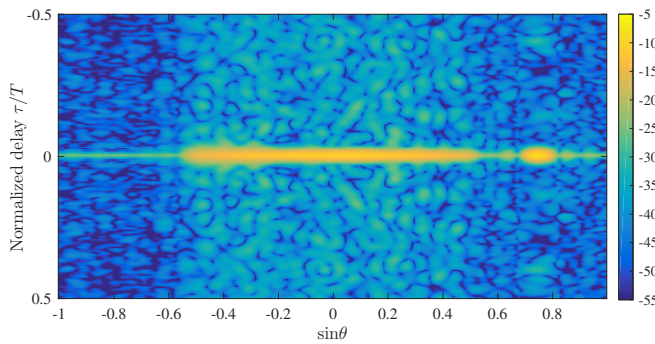


Fig. 25. Autocorrelation function for wideband (%BW = 40% bandwidth) wide beam + secondary beam MIMO emission versus  $\sin \theta$  for normalized delay  $\tau/T \in [-0.5, 0.5]$ .

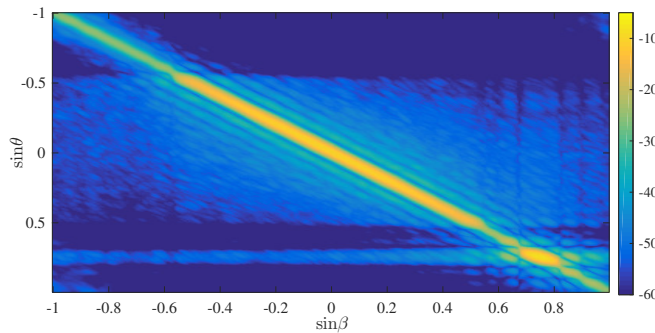


Fig. 26. Maximum angular cross-correlation for wideband (%BW = 40% bandwidth) wide beam + secondary beam MIMO emission as a function of  $\sin \theta$  and  $\sin \beta$  for an  $M = 30$  element ULA with  $f_d = f_{\text{cent}} + B/2$ .

level are comparable to a standard beamforming ambiguity function. The use of multiple proximate beamlets in the design of the wide beam results in enhanced spatial decorrelation and therefore an improvement in both spatial resolution and ambiguity sidelobe level.

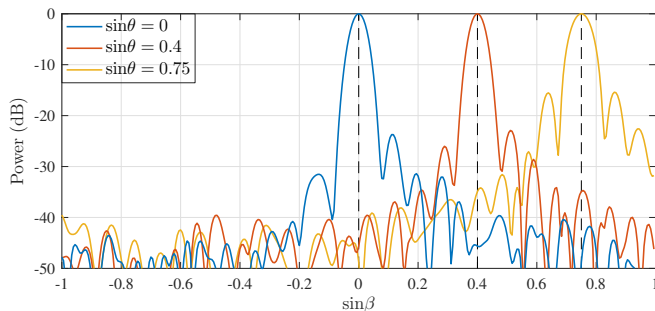


Fig. 27. Peak-normalized angle-delay ambiguity function at  $\tau/T = 0$  for wideband (%BW = 40% bandwidth) wide beam + secondary beam MIMO emission versus  $\sin \beta$  for the transmit angles  $\sin \theta = 0$  (blue) and  $\sin \theta = 0.4$  (red), directions within the wide beam, and  $\sin \theta = 0.75$  (yellow), the secondary beam direction.

The emission design cost function  $J(i)$  is shown in Fig. 28 versus iteration index  $i$  for versions with (blue) and without (red) the adaptive scaling. For both scenarios, convergence occurs within 40 iterations (and very nearly so after 15 iterations). The version using the adaptive scaling converges to a lower cost function solution. Fig. 29 shows the RUWO

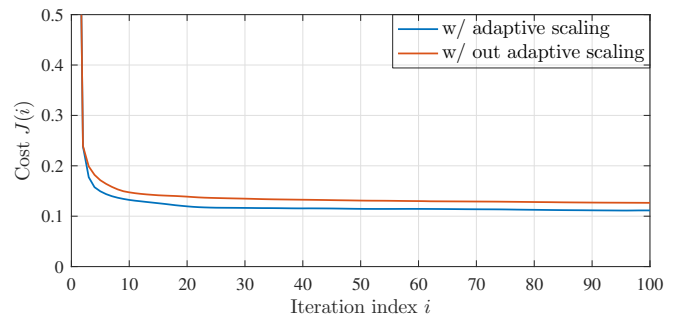


Fig. 28. Emission design cost function  $J(i)$  versus iteration index  $i$  ( $\Phi = 100$  iterations;  $K = 20$  nulling iterations) for wideband (%BW = 40% bandwidth) wide beam + secondary beam MIMO emission with adaptive scaling (blue) and without adaptive scaling (red) for an  $M = 30$  element ULA with  $f_d = f_{\text{cent}} + B/2$ .

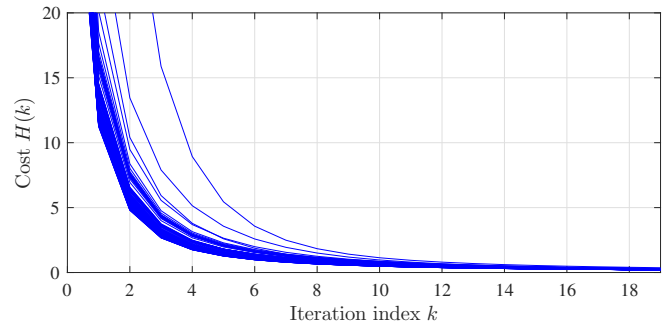


Fig. 29. RUWO cost function  $H(k)$  versus iteration index  $k$  ( $\Phi = 100$  iterations;  $K = 20$  nulling iterations) for wideband (%BW = 40% bandwidth) wide beam + secondary beam MIMO emission for an  $M = 30$  element ULA with  $f_d = f_{\text{cent}} + B/2$ .

cost function  $H(k)$  versus iteration index  $k$  for all  $\Phi = 100$  iterations. Again the cost  $H(k)$  decreases at each iteration.

## VII. CONCLUSION

An iterative, wideband MIMO optimization scheme for far-field emission design has been presented that optimizes the spectral content in certain predefined angles denoted as beamlets. Space-frequency nulling is also implemented inside the iterative process via the reiterative uniform-weight optimization (RUWO) method. The design process avoids placing power into the invisible space by maximizing power emitted into the visible space, thus avoiding large amounts of reactive power that would occur otherwise and that could potentially damage the radar. The resulting waveforms are constrained to be constant-modulus and can be implemented as continuous-time PCFM waveforms. Three different scenarios have been examined to show the versatility of the design scheme. The results demonstrate that for a randomized waveform initialization, the subsequent wide beam emission design provides greater spatial decorrelation, and thus finer spatial resolution and lower spatial ambiguity sidelobes than a narrow beam emission, though the latter can achieve better waveform autocorrelation properties (lower range sidelobes).

APPENDIX A  
BEAMLET CONSTRAINT FROM (29)

We want to constrain the available beamlet directions in  $\Theta_P$  such that the mainlobe of each beamlet is contained entirely within the visible domain (for in-band frequencies). The peak-to-null beamwidth  $W$  in  $\sin \theta$  space for a uniform linear array with  $M$  elements and inter-element spacing  $d$  is

$$W = \frac{c}{Mfd}.$$

Inserting the representation of  $d$  from (3) yields

$$W = \frac{2fd}{Mf}.$$

The widest beamwidth for in-band frequencies occurs at  $f = f_{\text{cent}} - B/2$ . Therefore the maximum peak-to-null beamwidth for in-band frequencies is

$$W_{\text{max}} = \frac{2f_d/f_{\text{cent}}}{M \left(1 - \frac{\%BW}{2}\right)}.$$

Bounding  $\sin \Theta_P$  such that each mainlobe within the set avoids the invisible domain for all in-band frequencies is thus

$$\sin \Theta_P \leq 1 - W_{\text{max}} = 1 - \frac{2f_d/f_{\text{cent}}}{M \left(1 - \frac{\%BW}{2}\right)}.$$

REFERENCES

- [1] M. Wicks, E. Mokole, S.D. Blunt, V. Amuso, and R. Schneible, eds., *Principles of Waveform Diversity & Design*, SciTech Publishing, 2010.
- [2] S. Pillai, K.Y. Lo, I. Selesnick, and B. Himed, *Waveform Diversity: Theory and Applications*, McGraw-Hill, 2011.
- [3] F. Gini, A. De Maio, and L.K. Patton, *Waveform Design and Diversity for Advanced Radar Systems*, IET Press, 2012.
- [4] S.D. Blunt and E.L. Mokole, "An overview of radar waveform diversity," *IEEE AES Systems Magazine*, Oct. 2016.
- [5] D.R. Fuhrmann and G.S. Antonio "Transmit beamforming for MIMO radar systems using signal cross-correlation," *IEEE Trans. Aerosp. Electron. Syst.*, vol. 44, no. 1, pp.1–16, Jan. 2008.
- [6] S. Ahmed, J.S. Thompson and B. Mulgrew, "Unconstrained synthesis of covariance matrix for MIMO radar transmit beampattern," *IEEE Trans. Signal Processing*, vol. 59, no. 8, pp. 3837–3849, Aug. 2011.
- [7] P. Stoica, J. Li and X. Zhu "Waveform synthesis for diversity-based transmit beampattern design," *IEEE Trans. Signal Process.*, vol. 56, no. 6, pp. 2593–2598, June 2008.
- [8] D.P. Scholnik and J.O. Coleman "Optimal design of wideband array patterns," *IEEE Intl. Radar Conf*, Washington, DC, May 2000.
- [9] D.P. Scholnik and J.O. Coleman "Optimal array-pattern synthesis for wideband digital transmit arrays," *IEEE Journal of Selected Topics in Signal Processing*, vol. 1, no. 4, pp. 660–677, Dec. 2007.
- [10] G.S. Antonio, D.R. Fuhrmann, "Beampattern synthesis for wideband MIMO radar systems," *IEEE Computational Advances in Multi-Sensor Adaptive Processing*, Puerto Vallarta, Mexico, pp. 105–108, Dec. 2005.
- [11] H. He, P. Stoica, and J. Li, "Wideband MIMO systems: signal design for transmit beampattern synthesis," *IEEE Trans. Signal Process.*, vol. 59, pp. 618–628, Feb. 2011.
- [12] P.M. McCormick, S.D. Blunt, and J.G. Metcalf, "Joint spectrum/beampattern design of wideband FM MIMO radar emissions," *IEEE Radar Conf.*, Philadelphia, PA, May 2016.
- [13] S.D. Blunt, M. Cook, J. Jakabosky, J. de Graaf, and E. Perrins, "Polyphase-coded FM (PCFM) waveforms: part I: implementation," *IEEE Trans. Aerospace & Electronic Systems*, vol. 50, no. 3, pp. 2218–2229, July 2014.
- [14] R.W. Gerchberg and W.O. Saxton, "A practical algorithm for the determination of the phase from image and diffraction plane pictures," *Optik*, vol. 35, no. 2, pp. 237–246. 1972.
- [15] A. Levi and H. Stark, "Image restoration by the method of generalized projections with application to restoration from magnitude," *J. Opt. Soc. Am.*, vol. 1, no. 9, pp. 932–943, Sept. 1984.
- [16] H.H. Bauschke and J.M. Borwein, "On projection algorithms for solving convex feasibility problems," *SIAM Review*, vol. 38, no. 3, pp. 367–426, Sept. 1996.
- [17] O.M. Bucci, G. Franceschetti, G. Mazzarella, and G. Panariello, "Intersection approach to array pattern synthesis," *IEE Proc. H Microwaves, Antennas and Propagation*, vol. 137, no. 6, pp. 349–357, Dec. 1990.
- [18] J.R. Fienup, "Phase retrieval algorithms: a comparison," *Applied Optics*, vol. 21, no. 4, pp. 2758–2769.
- [19] L.K. Patton and B.D. Rigling, "Phase Retrieval for Radar Waveform Optimization," *IEEE Trans. Aerosp. Electron. Syst.*, vol. 48, no. 4, pp. 3287–3302, Oct. 2012.
- [20] J. Jakabosky, S.D. Blunt, and B. Himed, "Waveform design and receive processing for nonrecurrent nonlinear FMCW radar," *IEEE Intl. Radar Conf.*, Washington, DC, May 2015.
- [21] J. Jakabosky, S.D. Blunt, and T. Higgins, "Ultra-low sidelobe waveform design via spectral shaping and LINC transmit architecture," *IEEE Intl. Radar Conf.*, Washington, DC, May 2015.
- [22] T. Higgins, T. Webster, A. K. Shackelford, "Mitigating interference via spatial and spectral nulling," *Radar, Sonar & Navigation, IET*, vol.8, no.2, pp.84–93, Feb. 2014.
- [23] G. Frazer, Y. Abramovich, and B. Johnson, "Spatially waveform diverse radar: perspectives for high frequency OTHR," *IEEE Radar Conf.*, pp. 385-390, Boston, MA, USA, 2007.
- [24] F. Daum and J. Huang, "MIMO radar: snake oil or good idea?" *IEEE Aerospace & Electronic Systems Mag.*, vol. 24, no. 5, pp. 8–12, May 2009.
- [25] D.R. Rhodes, "On the stored energy of planar apertures," *IEEE Trans. Antenna Propagation*, vol. 14, no. 6, pp. 676–683, Nov. 1964.
- [26] G. Krieger, "MIMO-SAR: opportunities and pitfalls," *IEEE Trans. Geoscience & Remote Sensing*, vol. 52, no. 5, pp. 2628–2645, May 2014.
- [27] G.C. Tavik, et al, "The advanced multifunction RF concept," *IEEE Trans. Microwave Theory & Techniques*, vol. 53, no. 3, pp. 1009–1020, Mar. 2005.
- [28] Allen, John L., and B.L. Diamond. *Mutual coupling in array antennas*. No. TR-424. Massachusetts Inst. of Tech. Lexington Lincoln Lab, 1966.
- [29] Allen, J.L. "On array element impedance variation with spacing," *IEEE Trans. Antennas and Propagation*, vol. 12, no. 3, pp. 371–372, May 1964.
- [30] Stutzman, Warren L., and Gary A. Thiele. *Antenna theory and design*. John Wiley & Sons, 2012.
- [31] Merrill, I. Skolnik. *Radar handbook*, 2nd ed. McGraw Hill, 1990.
- [32] B. Cordill, J. Metcalf, S.A. Seguin, D. Chatterjee, and S. D. Blunt, "The impact of mutual coupling on MIMO radar emissions," *IEEE Intl. Conf. EM in Advanced Applications*, Turino, Italy, pp. 644–647, Sept. 2011.
- [33] G. Babur, P.J. Aubry, and F. Le Chevalier, "Antenna coupling effects for space-time radar waveforms: analysis and calibration," *IEEE Trans. Antennas & Propagation*, vol. 62, no. 5, pp. 2572–2586, May 2014.
- [34] Van Trees, H. L., *Optimum Array Processing*, John Wiley & Sons, 2002, Chap. 2.
- [35] Smith, Steven W. *Digital signal processing: a practical guide for engineers and scientists*. Newnes, 2003.
- [36] J.D. Taylor, ed. *Introduction to ultra-wideband radar systems*. CRC press, 1994.
- [37] H. Griffiths, S. Blunt, L. Cohen, L. Savy, "Challenge problems in spectrum engineering and waveform diversity," *IEEE Radar Conference*, Ottawa, Canada, Apr./May 2013
- [38] H. Griffiths, L. Cohen, S. Watts, E. Mokole, C. Baker, M. Wicks, and S. Blunt, "Radar spectrum engineering and management: technical and regulatory issues," *Proceedings of the IEEE*, vol. 103, no. 1, pp. 85–102, Jan. 2015.
- [39] S.W. Frost, B. Rigling, "Sidelobe predictions for spectrally-disjoint radar waveforms," *IEEE Radar Conf. Atlanta, GA*, May 2012. pp. 247–252.
- [40] I.W. Selesnick, S.U. Pillai, R. Zheng, "An iterative algorithm for the construction of notched chirp signals," *2010 IEEE Radar Conf.* Washington, DC, May 2010. pp. 200–203.
- [41] I.W. Selesnick, S.U. Pillai, "Chirp-like transmit waveforms with multiple frequency-notches," *2011 IEEE Radar Conf.*, Kansas City, MO, May 2011, pp. 1106–1110.
- [42] J. Jakabosky, B. Ravenscroft, S.D. Blunt, and A. Martone, "Gapped spectrum shaping for tandem-hopped radar/communications & cognitive sensing" *IEEE Radar Conf.*, Philadelphia, PA, May 2016.
- [43] J.A. Johnston and A.C. Fairhead, "Waveform design and Doppler sensitivity analysis for nonlinear FM chirp pulses," *IEE Proc. Communications, Radar & Signal Processing*, vol. 133, no. 2, pp. 163–175, Apr. 1986.

- [44] S.D. Blunt, P.M. McCormick, T. Higgins, and M. Rangaswamy, "Physical emission of spatially-modulated radar," *IET Radar, Sonar and Navigation*, vol. 8, no. 9, pp. 1234–1246, Dec. 2014.



**Patrick M. McCormick** (S'12) received his B.S. in mechanical engineering in 2008 and B.S. electrical engineering in 2013 from the University of Kansas. He is currently pursuing a Ph.D. degree in electrical engineering from the University of Kansas on radar systems and signal processing.

His research interests include adaptive receive processing, design of alternative radar transmission schemes, including spatial and polarization diverse emissions.



**Shannon D. Blunt** (S'96–M'02–SM'07) received the Ph.D. degree in electrical engineering from the University of Missouri in 2002. From 2002 to 2005 he was with the Radar Division of the Naval Research Laboratory in Washington, D.C. Since 2005 he has been with the Department of Electrical Engineering and Computer Science at the University of Kansas where he is currently a Professor and Director of the Radar Systems & Remote Sensing Lab (RSL).

In 2012 Prof. Blunt received the IEEE/AESS Nathanson Memorial Radar Award and in 2008 received the AFOSR Young Investigator Award. He has over 120 refereed journal and conference publications, 11 patents, 7 book chapters, and co-edited the book *Principles of Waveform Diversity & Design*.

He is a member of the IEEE/AESS Radar Systems Panel where he is currently Chair of the Conferences Committee. He is an Associate Editor for *IEEE Transactions on Aerospace & Electronic Systems* and is on the Editorial Board for *IET Radar, Sonar & Navigation*. He was General Chair of the 2011 IEEE Radar Conference in Kansas City and is a member of the program committee for the MSS Tri-Service Radar Symposium series. He was Chair of the NATO SET-179 research task group on "Dynamic Waveform Diversity & Design" and a member of SET-182 on "Radar Spectrum Engineering & Management" and SET-227 on "Cognitive Radar". He is a Fellow of IEEE.



**Justin G. Metcalf** (S'08) received his Bachelor's degree in Computer Engineering from Kansas State University in 2006 where he was selected as a National Merit Scholar and a KSU Presidential Scholar in 2001. From 2006-2008 he was at the Flight Simulation Labs of Lockheed Martin Aeronautics in Fort Worth, TX. From 2008-2014 he was at the Radar Systems Lab of the University of Kansas, where he obtained a Master's degree in Electrical Engineering (with Honors) in 2011 and the Ph.D. degree in Electrical Engineering (with Honors) in

2015. He was the recipient of the Richard and Wilma Moore Award for the best departmental Master's thesis in 2011-2012. He has been a Research Electronics Engineer with the Sensors Directorate of the Air Force Research Laboratory since November of 2014. He is the chair of the Dayton Chapter of the IEEE Aerospace and Electronic Systems Society. His interests are cognitive radar, waveform design, detection theory, statistical signal processing, game theory, and multi-function RF systems.